Electronic supplementary information (ESI)

# Pyrolysis of an amorphous cobalt(II) cubane-like coordination polymer towards tunable structurally disordered materials

*Sara Frank[1], Mads Folkjær[1], Melissa J. Marks[1], Simon J. L. Billinge[2], and Nina Lock[3]**

[1]Department of Biological and Chemical Engineering, Aarhus University

Åbogade 40, 8200 Aarhus N, Denmark

[2]Department of Applied Physics and Applied Mathematics, Columbia University

New York 10027, United States

[3]Department of Biological and Chemical Engineering and Interdisciplinary Nanoscience Center (iNANO), Aarhus University, Åbogade 40, 8200 Aarhus N, Denmark

*Corresponding author: Nina Lock (nlock@bce.au.dk)

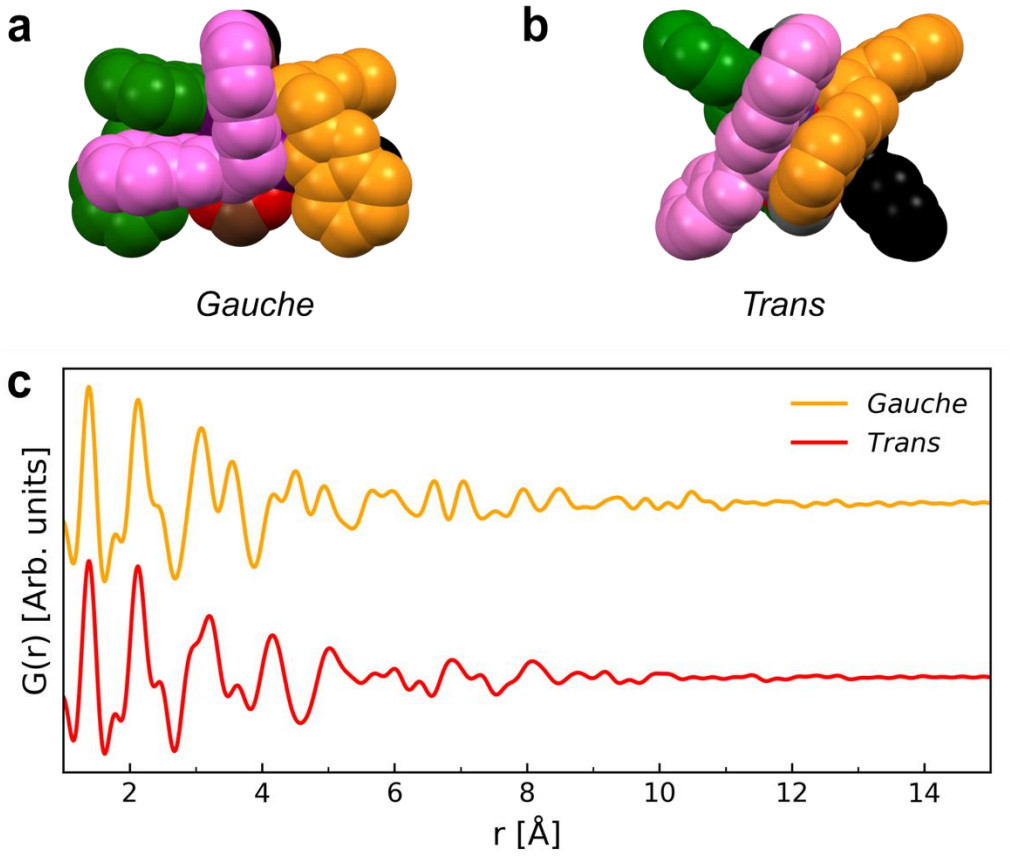


**Fig. S1.** Cluster conformations based on the published crystal structures.[1] a) *Gauche* cluster (CCDC 1983936) and b) *trans* cluster (CCDC 1983937). Each colour represents one bisbenzimidazole ligand c) Debye calculation of the two cluster conformations, performed with Diffpy-CMI.[2]

| Cluster refinement | *delta2* | *zoomscale* | *Trans/Gauche* | $R_w$ (%) |
|---|---|---|---|---|
| Cobalt(II) cubane | 2.91 | 1.00347 | 0.68/0.32 | 32.2 |

**Table S1.** Refined parameters from cluster refinement in DiffPy-CMI to *ex situ* cobalt(II) cubane data (Fig. S2) against the *trans* and *gauche* clusters presented in Fig. S1a,b. The scale factor, a parameter that allows for the clusters to expand or contract (*zoomscale*), and a parameter accounting for the correlated motion (*delta2*) were refined, and in that order. The *zoomscale* and *delta2* parameters were constrained to take the same values for the two clusters. Atomic displacement parameters (ADPs) were fixed to minimize the number of variables, to $B_{iso,Co}$ = 2 Å$^2$ and $B_{iso,CNO}$ = 0.2 Å$^2$ based on initial refinements. The PDF was generated with xPDFsuite[3] and with $Q_{max}$ = 21.4 Å$^{-1}$ and $Q_{min}$ = 1.0 Å$^{-1}$ (to remove the modulation from packing of the CP). The instrumental parameters of $Q_{damp}$ = 0.03527 Å$^{-1}$ and $Q_{broad}$ = 0.016149 Å$^{-1}$ were determined based on refinement of a Si standard. The fit is displayed in Fig. 1e in the main text.

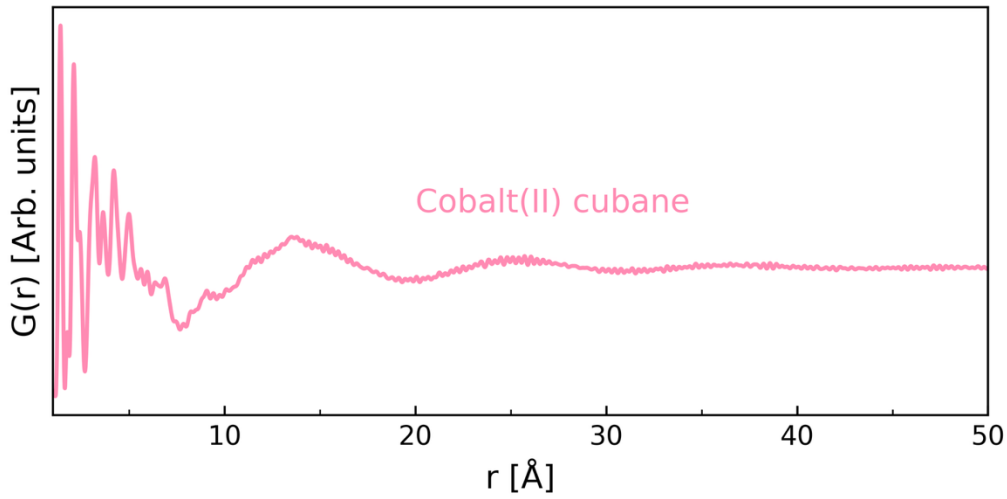


**Fig. S2.** PDF data of the cobalt(II) cubane; $Q_{max}$ = 21.4 Å$^{-1}$ and $Q_{min}$ = 0.1 Å$^{-1}$.

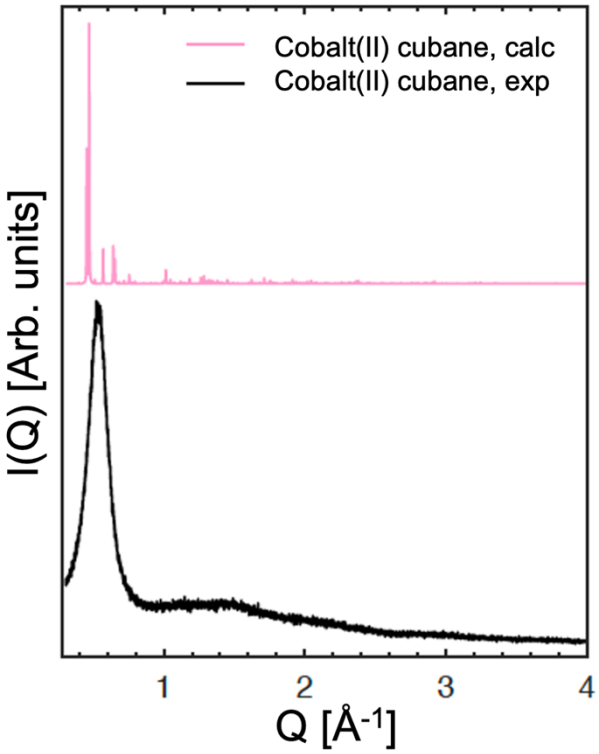


**Fig. S3.** XRD on as-synthesized cobalt(II) cubane, denoted 'exp', collected on a Rigaku Smarlab diffractometer using Co $K\alpha_1$ and $K\alpha_2$ radiation ($\lambda$ = 1.79 Å), compared with the calculated pattern, denoted 'calc', based on the published crystal structure (CCDC 1983936).[1]

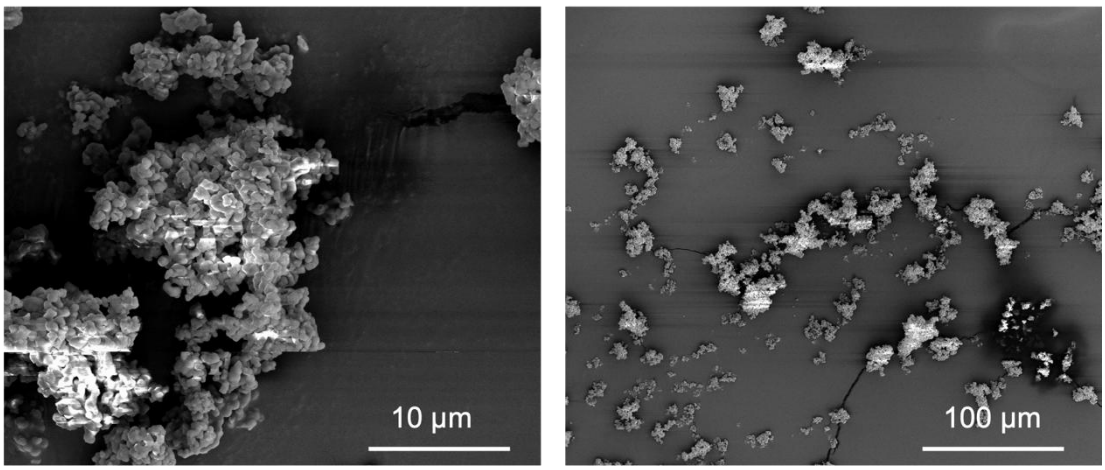


**Fig. S4.** SEM on the as-synthesized cobalt(II) cubane powder. Images were obtained on a FEI-Nova NanoSEM 600 under high vacuum conditions. The sample was coated with a 6.0 nm Pt layer using a LEICA EM SCD 500 vacuum-film-deposition system equipped with a LEICA EM QSG100 Quartz Crystal Film Thickness Monitor; however, charging is still visible.

## STEM-EDX and 4D-STEM investigations

### Experimental

4D-STEM and STEM-EDX measurements were carried out using a FEI Talos FX-200 electron microscope operating at 200 kV. The samples were prepared by dispersing ground powders in absolute ethanol and subsequently ultrasonicating. 3 × 5 µL of the dispersion was drop-cast onto ultrathin carbon film on lacey carbon, 400M, Max H7, Cu grids. The prepared grids were mounted in a single tilt holder. STEM images were acquired using a high-angle annular dark field (HAADF) detector at a camera length of 98 mm, giving a collection angle range of 66-200 mrad. The beam convergence angle was 10.5 mrad and FWHM 0.29 nm, neglecting chromatic and higher-order aberrations.

4D-STEM data was acquired using a Merlin 4R hybrid pixel detector from Quantum Detectors, using only one chip, resulting in each diffraction pattern being collected on a detector with 256 × 256 pixels. A C2 aperture of 20 µm was used in nanoprobe mode, resulting in a convergence angle of 3.00 mrad and a beam FWHM of approximately 1.03 nm, ignoring chromatic and other higher-order aberrations. The camera length was 125 mm and the step size ~1.0 – 2.5 nm.

EDX data was collected using the ChemiSTEM Gen1 system installed on the same microscope. The EDX data was analyzed and plotted using the HyperSpy[4] and the eeee (easy EDX expy extension)[5] Python packages, using linear interpolation to remove the background and create characteristic X-ray line count maps. An 8x8 binning of the STEM-EDX data was used to make the elemental maps.

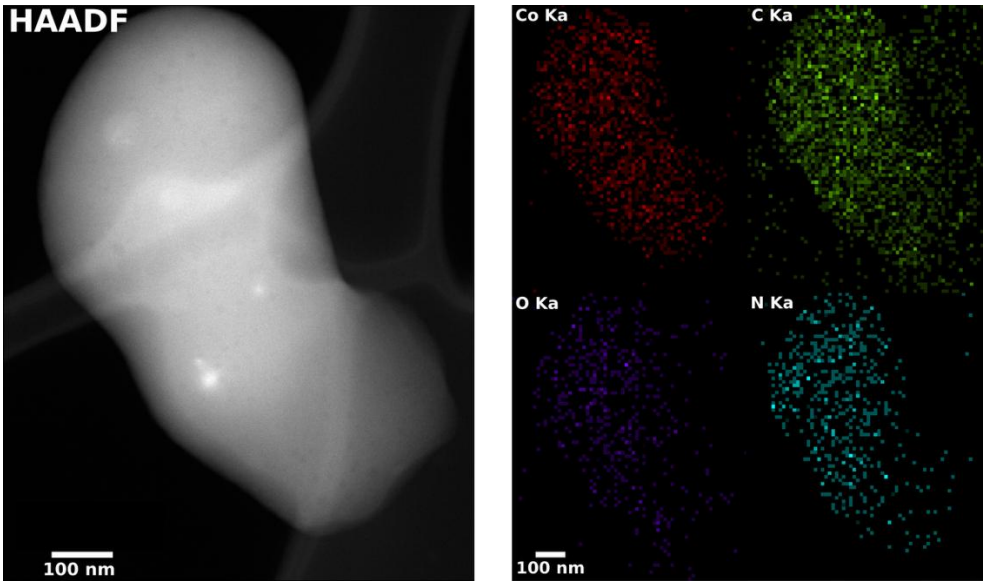


**Fig. S5.** STEM-EDX of the 450 °C/ 0 h pyrolyzed sample. Left HAADF image and right EDX-maps of Co Kα (red), C Kα (green), O Kα (purple), and N Kα (turquoise). A homogeneous distribution of elements is observed.

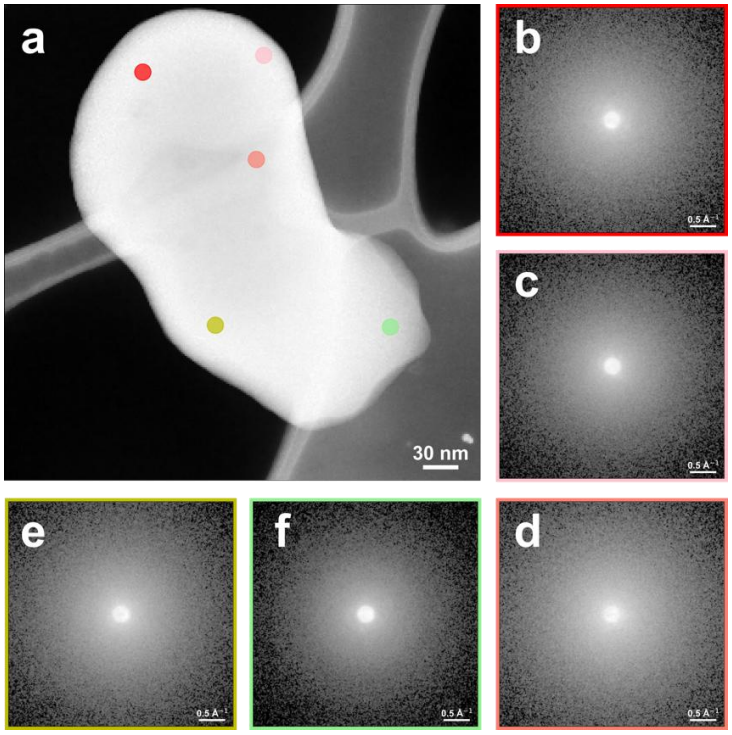


**Fig. S6.** 4D-STEM on the 450 °C/ 0 h pyrolyzed sample. a) Virtual ADF image, representing the integrated intensity over a *k*-range of 0.25–0.59 $Å^{-1}$. Selected points marked by colored circles correspond to the position of the diffraction patterns in the colored frames in b-f). All recorded diffraction patterns indicate an amorphous sample.

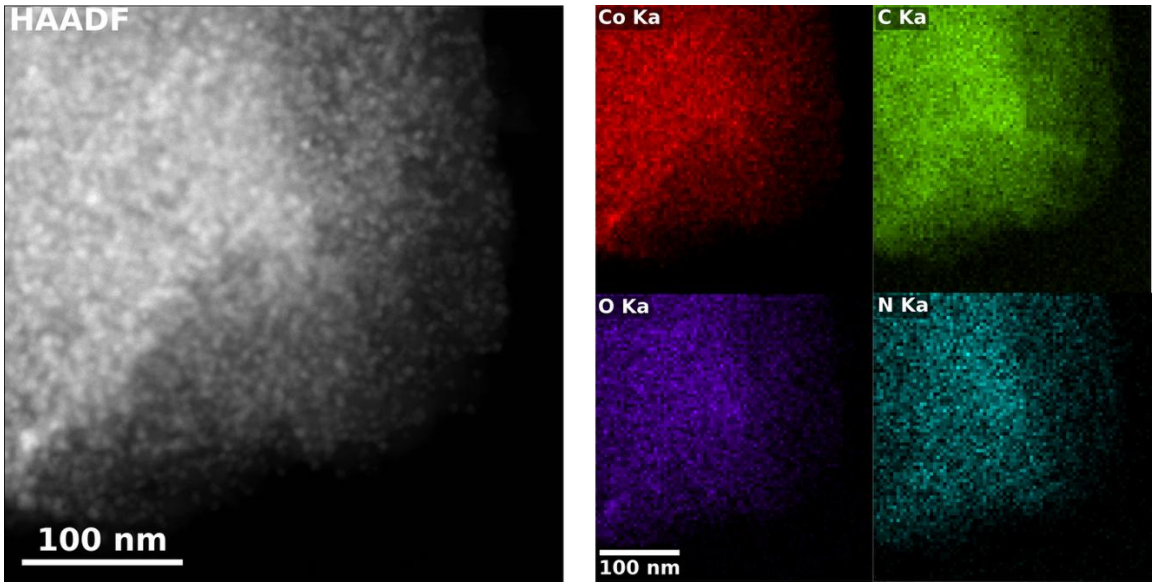


**Fig. S7.** STEM-EDX of the 500 °C/ 8 h pyrolyzed sample. Left HAADF image and right EDX-maps of Co Kα (red), C Kα (green), O Kα (purple), and N Kα (turquoise). The formation of embedded nanoparticles and clusters with an average size estimated to be 4.9 (4) nm from 100 measured particles is observed.

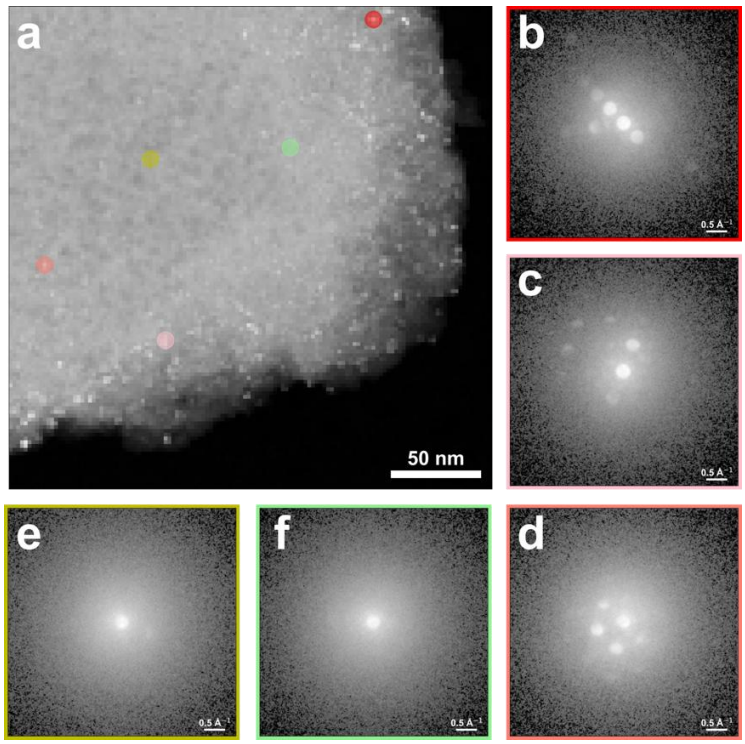


**Fig. S8.** 4D-STEM on the 500 °C/ 8 h pyrolyzed sample. a) Virtual ADF image, representing the integrated intensity over a *k*-range of 0.33–0.76 $Å^{-1}$. Selected points marked by colored circles correspond to the position of the diffraction patterns in the colored frames in b-f). b-d) Diffraction patterns at representative positions where Bragg disks are observed, indicating small crystals. e-f) Diffraction patterns indicating amorphous regions.

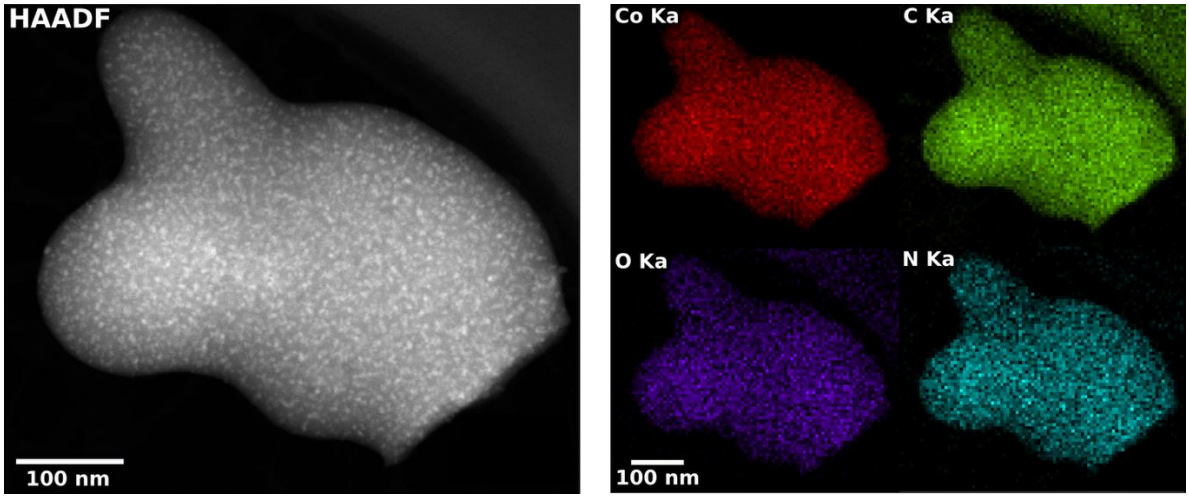


**Fig. S9.** STEM-EDX of the 500 °C/ 12 h pyrolyzed sample. Left HAADF image and right EDX-maps of Co Kα (red), C Kα (green), O Kα (purple), and N Kα (turquoise). The formation of embedded nanoparticles and clusters with an average size estimated to be 5.0 (5) nm from 100 measured particles is observed.

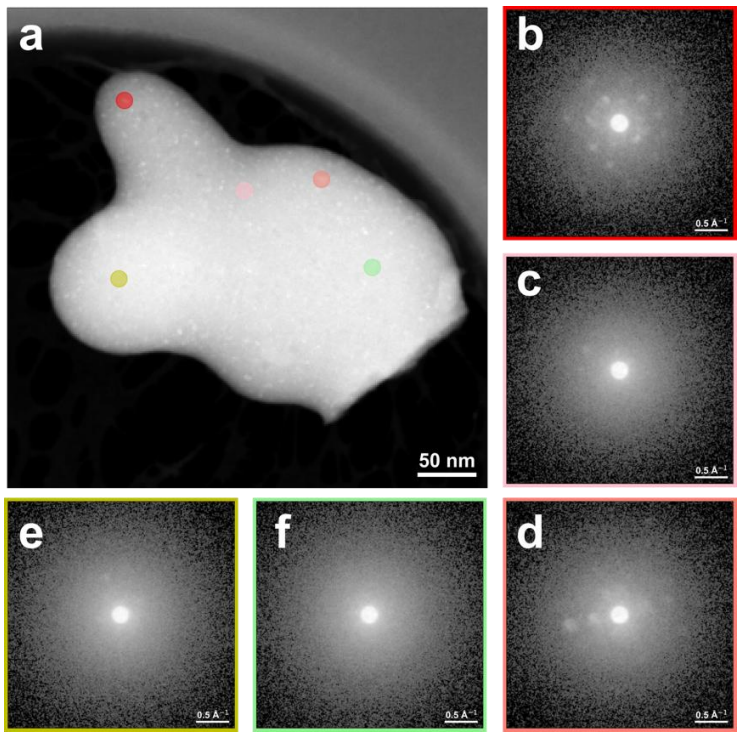


**Fig. S10.** 4D-STEM on the 500 °C/ 12 h pyrolyzed sample. a) Virtual ADF image, representing the integrated intensity over a *k*-range of 0.25–0.59 $Å^{-1}$. Selected points marked by colored circles correspond to the position of the diffraction patterns in the colored frames in b-f). b-d) Diffraction patterns at representative positions where Bragg disks are observed, indicating small crystals. e-f) Diffraction patterns indicating amorphous regions.

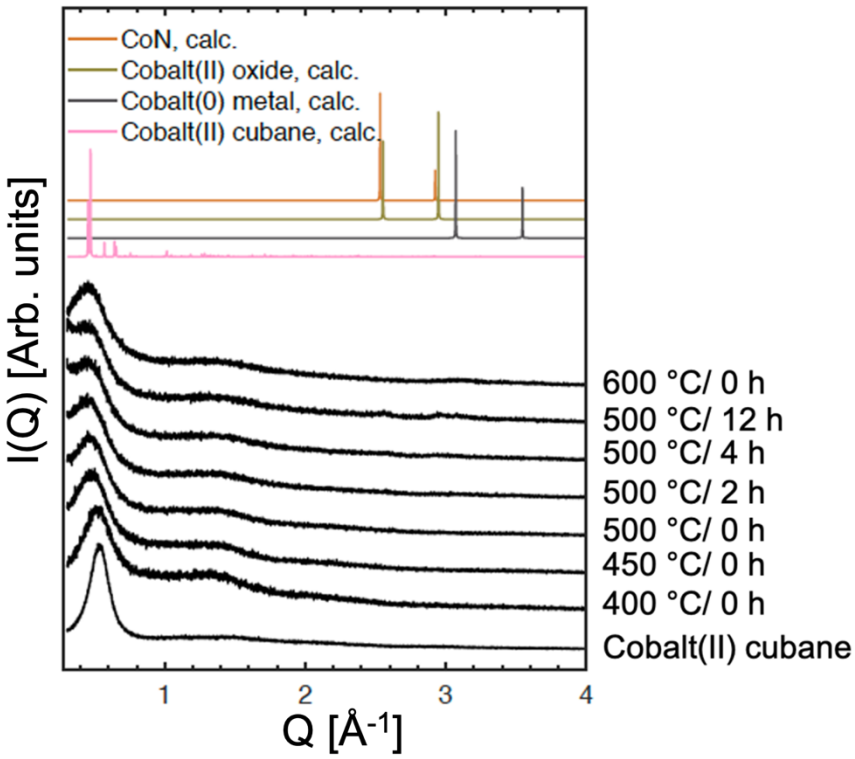


**Fig. S11.** XRD data on the pyrolyzed cobalt(II) cubane samples, collected on a Rigaku Smarlab diffractometer using Co $K\alpha_1$ and $K\alpha_2$ radiation ($\lambda$ = 1.79 Å), compared with the calculated patterns of cobalt(II) cubane (CCDC 1983936),[1] metallic cobalt (ICSD 76632),[6] cobalt(II) oxide (ICSD 9865),[7] and cobalt(II) nitride (ICSD 79936).[8]

| MOF/CP | Metal atom(s) | Linker | Initial crystallinity* | Pyrolysis conditions (Temperature range/ gas) | Decomposition product | Product crystallinity* | Ref |
|---|---|---|---|---|---|---|---|
| Cobalt(II) cubane<br><br>1D CP | Co | bdc=1,4-benzenedi-carboxylate | Amorphous | 400–600 °C (without and with isothermal hold at 500 °C)/ $N_2$ | Co metal and Co oxide NPs in carbon matrix | Mild pyrolysis: amorphous<br><br>Heavy pyrolysis: nanocrystalline | This work |
| Co-bdc<br><br>MOF | Co | bdc | Crystalline | 600 °C/ Ar | Co NPs in carbon matrix | Crystalline | [9] |
| ZIF-67<br><br>MOF | Co | 2-methyl-imidazola (2-mIm) | Crystalline | 550–650 °C (with and without isothermal hold)/ $N_2$ | Co NPs in N-doped carbon matrix | Crystalline | [10] |
| ZIF-8<br><br>MOF | Zn | 2-mIm | Crystalline | 300–900 °C/ $N_2$ | Carbon-ZnO composite | Crystalline | [11] |
| HKUST-1<br><br>MOF | Cu | btc = 1,3,5-benzenetri-carboxylate | Crystalline | RT–500 °C/ $N_2$ | Cu NPs in carbon matrix | Crystalline | [12] |
| Ni(bdc)(PNO)<br><br>MOF | Ni | bdc and PNO = pyridine-N-oxide | Crystalline | 342 °C, 375 °C, 411 °C, and 500 °C/ He *vs.* 10% $H_2$/He | Ni NPs surrounded by carbon shell | Crystalline | [13] |
| PCN-250<br>PCN = porous coordination network | Fe<br>$Fe_2Co$<br>$Fe_2Ni$ | 3,3′,5,5′-azobenzene-tetra-carboxylate | Crystalline | 200–380 °C with isothermal hold/ 3.5% $H_2$/He | Defect rich metal oxide NPs | Crystalline | [14] |

**Table S2.** Comparison of the crystallinity and decomposition product of the pyrolyzed cobalt(II) cubane with other pyrolyzed and thermally treated MOF and CPs in a comparable temperature range (< 1000 °C). It is noted that the literature in this field is extensive and that this table represents selected systems chosen mainly from studies focusing on fundamental principles, where the thermally induced structural transformation is followed with X-ray-based characterization techniques. Studies reporting on crystalline-amorphous phase transitions and not decompositions are not included, e.g. the field of glass-like MOFs.

**Based on the presence of discernable Bragg peaks in the scattered X-ray intensity signal I(Q). The 'heavy pyrolysis' samples from this work, where Bragg peaks were only captured in the normalized total scattering data and the 4D-STEM data, are assigned as nanocrystalline.*

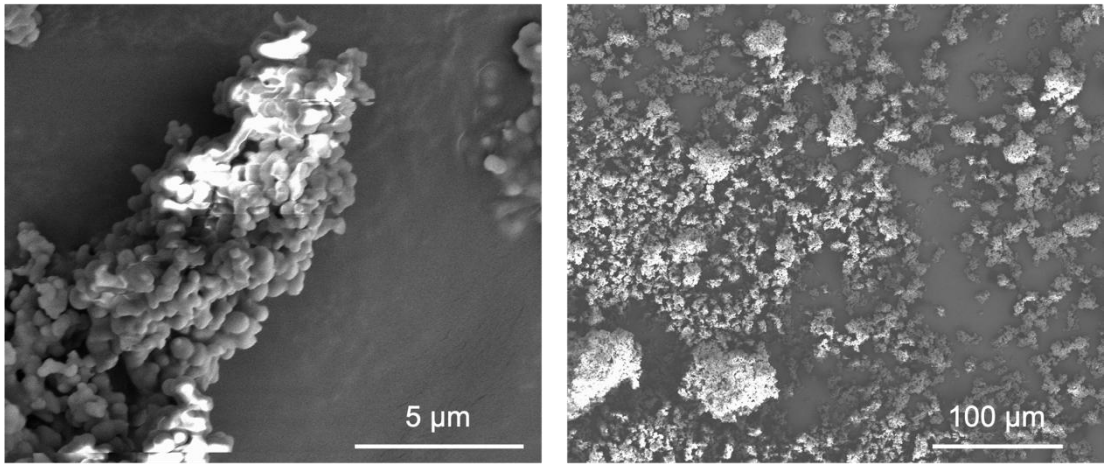


**Fig. S12.** SEM images of the 600 °C/ 0 h pyrolyzed sample. Images were obtained on a FEI-Nova NanoSEM 600 under high vacuum conditions. The sample was coated with a 6.0 nm Pt layer using a LEICA EM SCD 500 vacuum-film-deposition system equipped with a LEICA EM QSG100 Quartz Crystal Film Thickness Monitor.

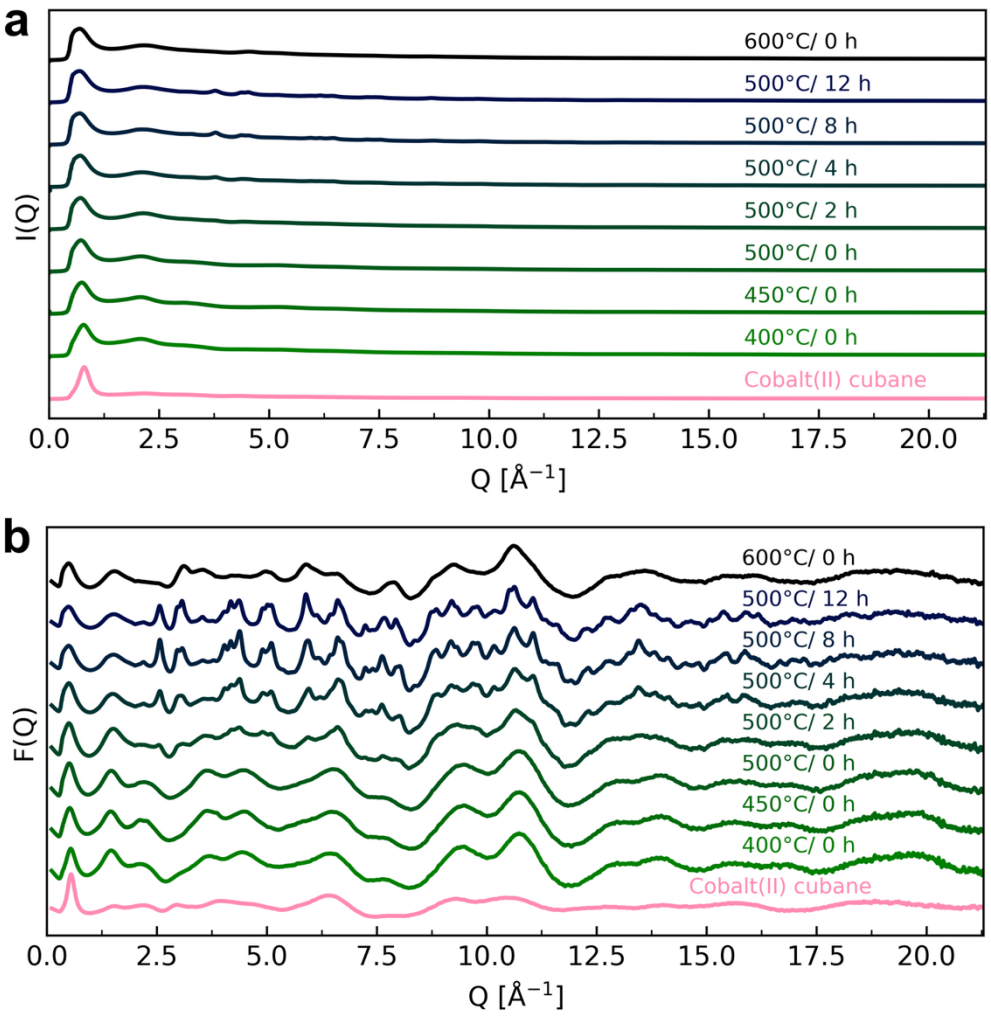


**Fig. S13.** Total scattering data of the pyrolysis series presented as a) *I*(*Q*) and b) *F*(*Q*).

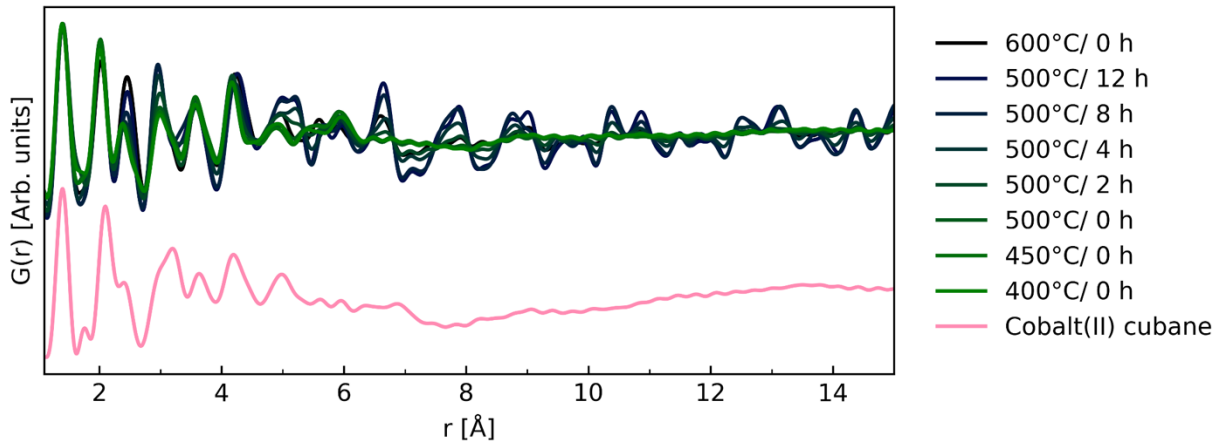


**Fig. S14.** PDFs in the local range.

| **500 °C/ 2 h**<br>**$R_w$ = 60.6 %** | Fraction<br>[atomic%] | *a=b=c*<br>[Å] | *Size*<br>[nm] | $U_{iso}$<br>Co(0) or Co(II) | $U_{iso}$<br>Co(III) | $U_{iso}$<br>O |
|---|---|---|---|---|---|---|
| Co | 97.3 | 3.567 | 1.1 | 0.2105 | - | - |
| CoO | 1.5 | 4.238 | 2.9 | 0.0132 | - | 0.0336 |
| $Co_3O_4$ | 1.1 | 8.104 | 3.7 | 0.0130 | 0.0063 | 0.0210 |
| **500 °C/ 4 h**<br>**$R_w$ = 35.2 %** | Fraction<br>[atomic%] | *a=b=c*<br>[Å] | *Size*<br>[nm] | $U_{iso}$<br>Co(0) or Co(II) | $U_{iso}$<br>Co(III) | $U_{iso}$<br>O |
| Co | 90.6 | 3.556 | 1.1 | 0.1286 | - | - |
| CoO | 4.9 | 4.238 | 2.9 | 0.0134 | - | 0.0363 |
| $Co_3O_4$ | 4.4 | 8.095 | 4.5 | 0.0101 | 0.0055 | 0.0177 |
| **500 °C/ 8 h**<br>**$R_w$ = 30.6 %** | Fraction<br>[atomic%] | *a=b=c*<br>[Å] | *Size*<br>[nm] | $U_{iso}$<br>Co(0) or Co(II) | $U_{iso}$<br>Co(III) | $U_{iso}$<br>O |
| Co | 7.9 | 3.548 | 3.8 | 0.0122 | - | - |
| CoO | 28.3 | 4.246 | 5.5 | 0.0093 | - | 0.0191 |
| $Co_3O_4$ | 63.7 | 8.097 | 4.5 | 0.0096 | 0.0057 | 0.0141 |
| **500 °C/ 12 h**<br>**$R_w$ = 31.3 %** | Fraction<br>[atomic%] | *a=b=c*<br>[Å] | *Size*<br>[nm] | $U_{iso}$<br>Co(0) or Co(II) | $U_{iso}$<br>Co(III) | $U_{iso}$<br>O |
| Co | 8.6 | 3.543 | 5.9 | 0.0071 | - | - |
| CoO | 30.0 | 4.246 | 5.5 | 0.0093 | - | 0.0199 |
| $Co_3O_4$ | 61.7 | 8.010 | 3.5 | 0.0097 | 0.0075 | 0.0014 |

**Table S3.** Refined parameters from three-phase PDF refinements performed in the range of 7.3-50 Å in PDFgui.[15] The parameter for correlated motion *delta2* was fixed at 4.0 for all phases, based on initial refinements.

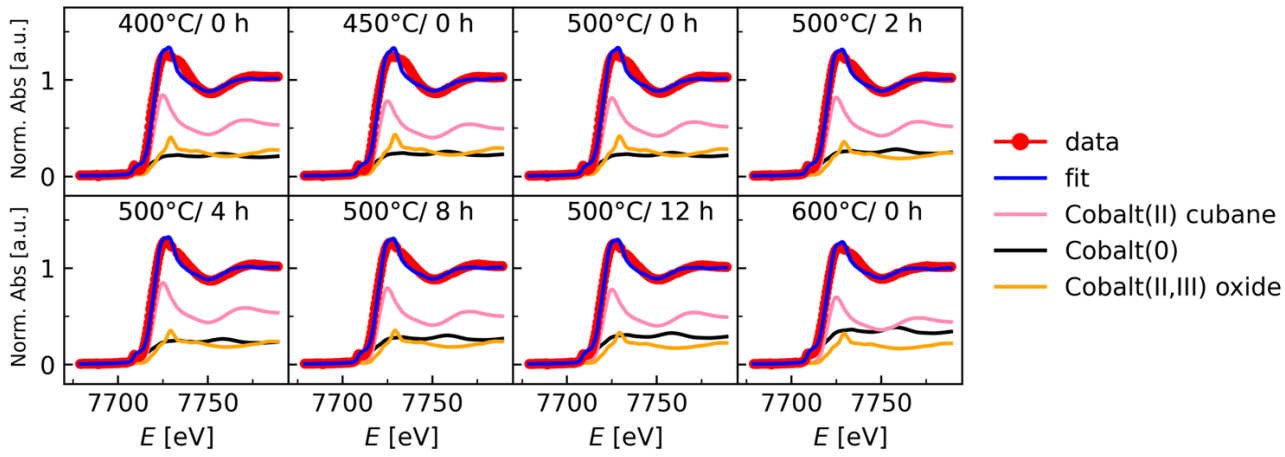


**Fig. S15.** LCA fits to *ex situ* XANES data for each of the pyrolyzed samples against cobalt(II) cubane, cobalt(0), and cobalt(II,III) oxide reference compounds.

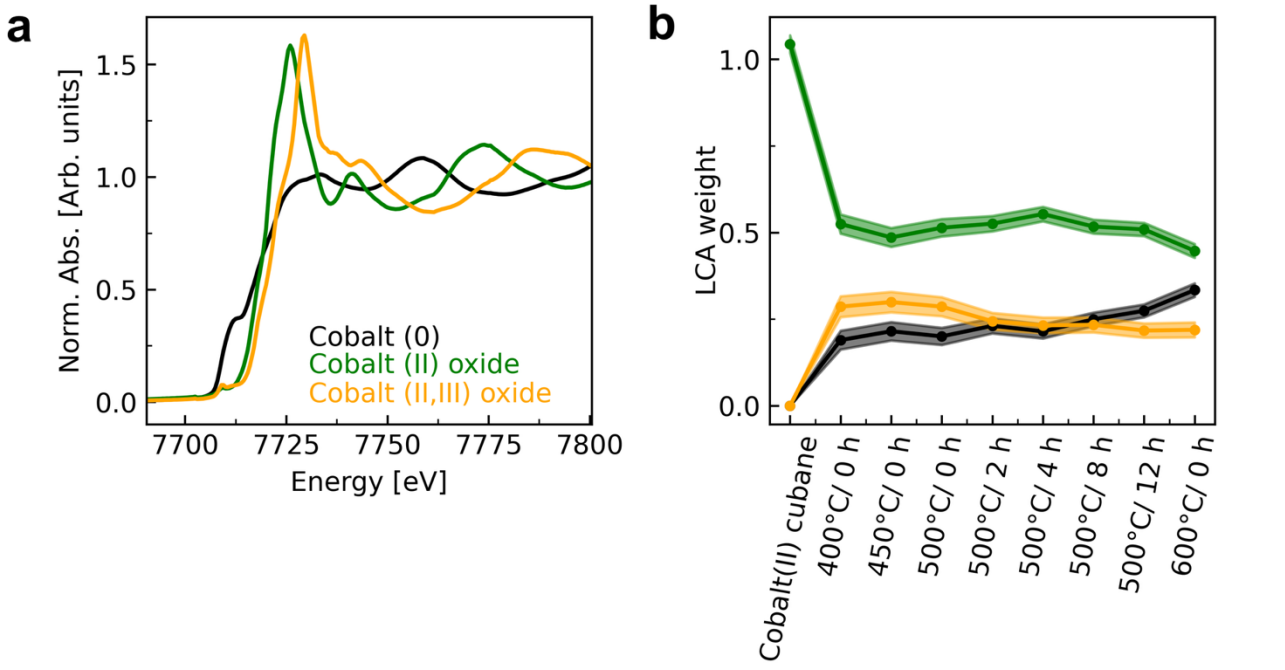


**Fig. S16.** LCA fits against cobalt(0), cobalt(II) oxide, and cobalt(II,III) oxide reference compounds. a) XANES spectra of the three reference compounds and b) the evolution of weight fractions.

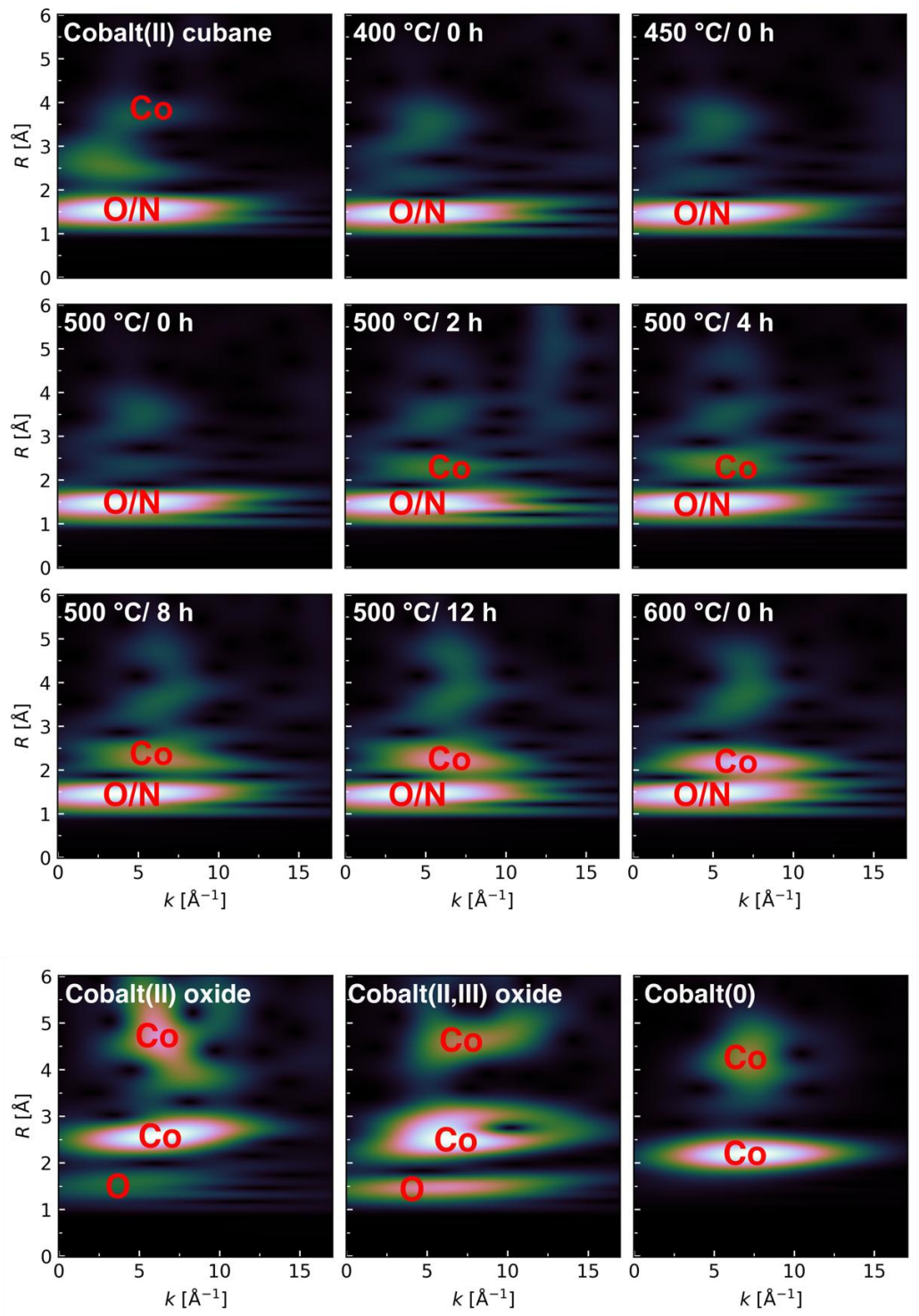


**Fig. S17.** Cauchy wavelet transforms[16] of the *ex situ* EXAFS spectra. The wavelet intensity at low *k* and short *R* (1–1.6 Å) is assigned to the light O/N back-scatterers from the cubane ligands, whereas the intensity centered at higher *k* and longer *R* (2.3–2.8 Å) is attributed to the heavier Co back-scatterers. Upon heating to 400 °C and 500 °C, the signals are dominated by the O/N domain. At the 500 °C isotherm, higher *k* Co features appear and grow monotonically with duration (4 h to 12 h). This is consistent with nucleation and growth of Co-rich domains. The Co signal is most intense for the 600 °C/ 0 h sample, indicating reduction and partial loss of the O/N coordination environment. The corresponding wavelet transforms of the three reference compounds are included for comparison.

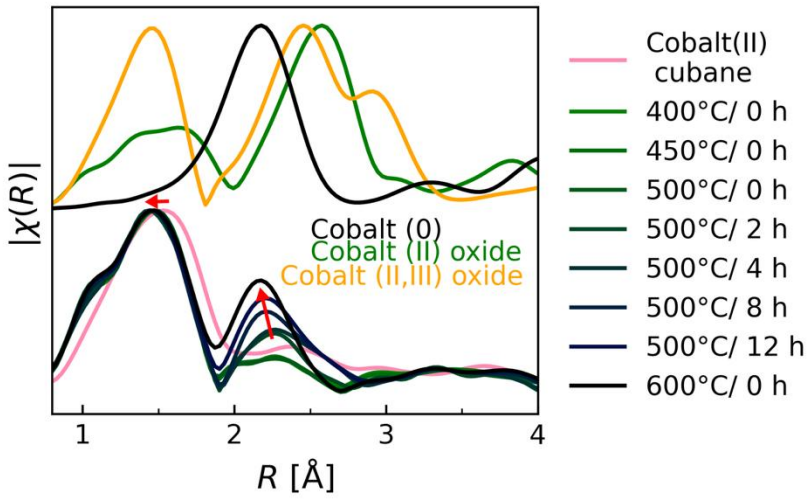


**Fig. S18.** Fourier transform of the *ex situ* EXAFS data on the pyrolyzed samples, plotted on top of each other.

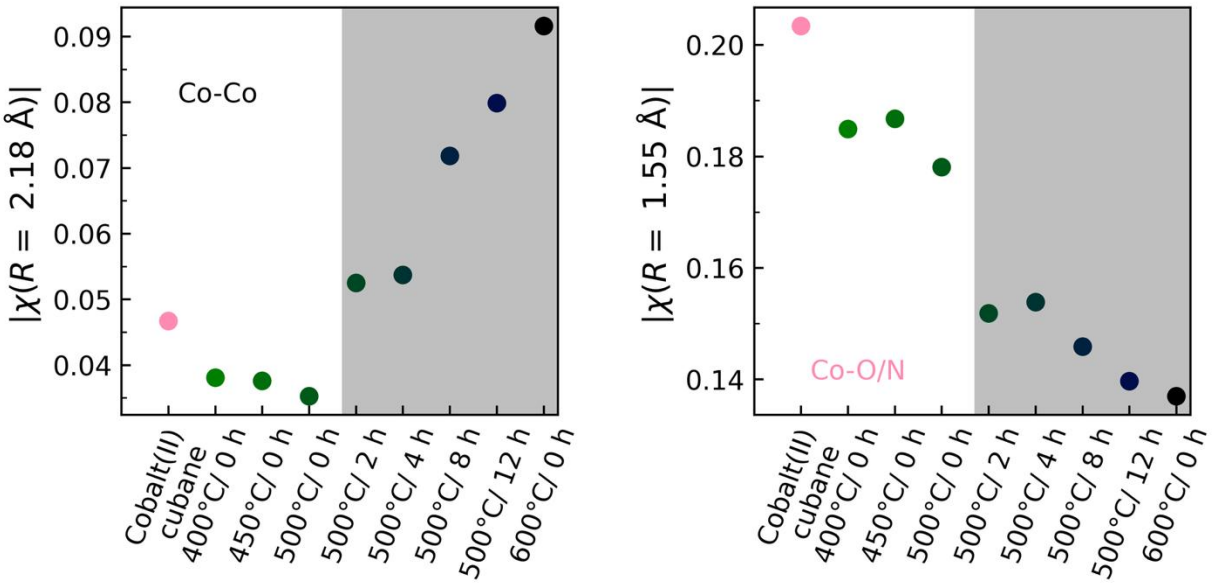


**Fig. S19.** Intensity evolution of nearest neighbor interactions from *ex situ* EXAFS. a) The Co–O/N interaction at 2.18 Å and b) The Co–Co interaction at 1.55 Å. The grey area indicates the 500 °C isotherm.

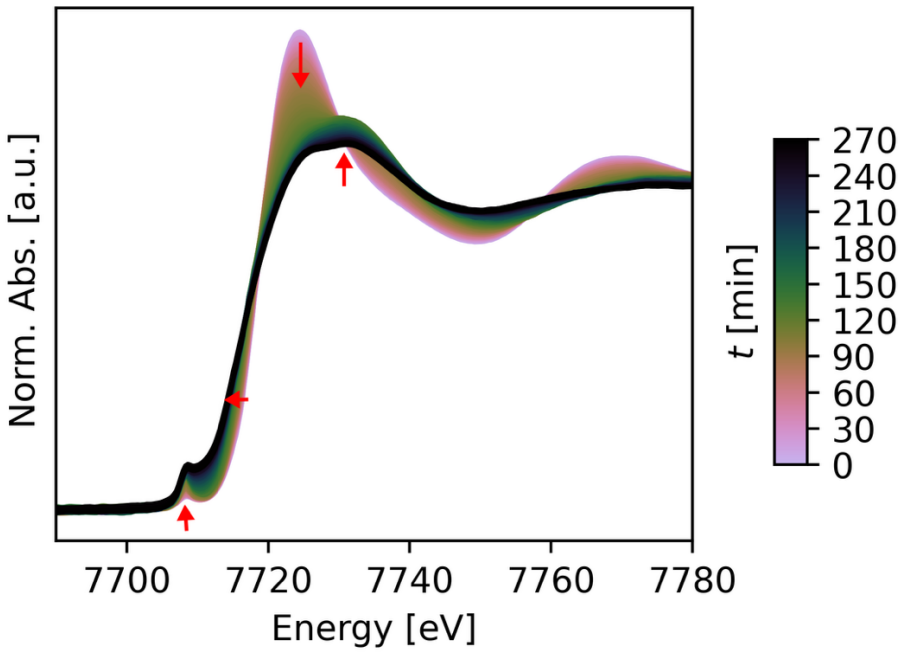


**Fig. S20.** XANES during *in situ* pyrolysis plotted on-top of each other with red arrows indicating regions of change.

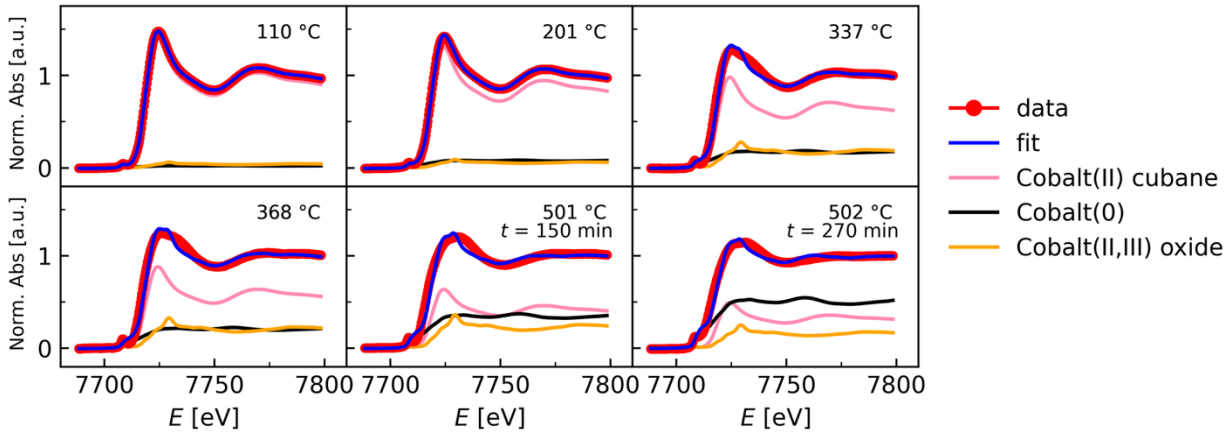


**Fig. S21.** LCA fits to *in situ* XANES data at six different temperatures/times.

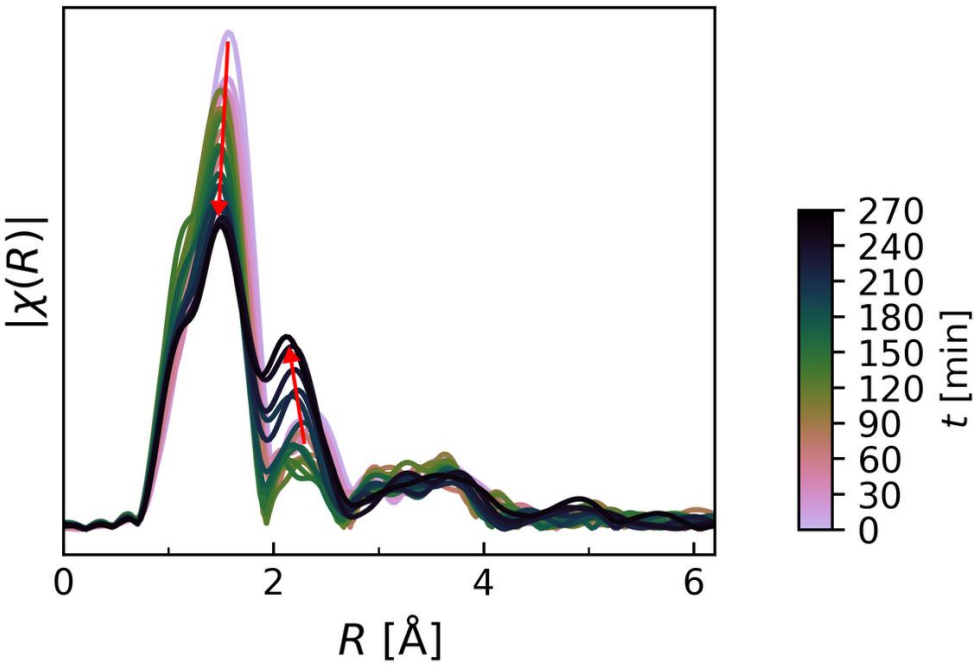


**Fig. S22.** EXAFS during *in situ* pyrolysis plotted on top of each other with red arrows indicating regions of change.

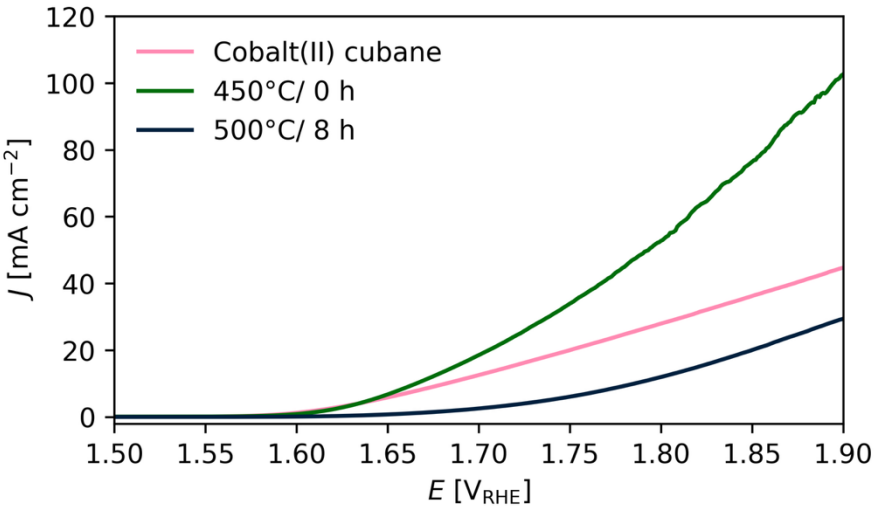


**Fig. S23** LSV of three materials, i.e. the pristine cobalt(II) cubane and samples pyrolyzed at 450 °C/ 0 h and 500 °C/ 8 h, in 1 M $KOH_{(aq)}$ with a scan rate of 10 mV $s^{-1}$ in an H-cell separated by a glass-frit with Pt as the counter electrode. While Pt dissolution and redeposition cannot be entirely excluded, the use of Pt as a cathode under alkaline conditions combined with short LSV scans, significantly limits this possibility. As all samples were tested under identical conditions, any minor contribution would not be expected to alter the observed relative activity trends. The overpotentials reported in the main text were assessed at $J$ = 10 mA $cm^{-2}$ with the standard reduction potential of the OER of $E^0$ = 1.288 $V_{RHE}$.

References


1. C. Deville, M. Folkjær, P. Reinholdt, M. S. Hvid, P. Lamagni, K. Borup, Z. Z. Sun, J. V. Lauritsen, V. McKee, K. M. O. Jensen and N. Lock, *Nanoscale*, 2020, **12**, 11601–11611.
2. P. Juhas, C. L. Farrow, X. H. Yang, K. R. Knox and S. J. L. Billinge, *Acta Crystallogr A*, 2015, **71**, 562–568.
3. X. Yang, P. Juhas, C. L. Farrow and S. J. Billinge, *arXiv preprint arXiv:1402.3163*, 2014.
4. F. de la Peña, E. Prestat, J. Lähnemann, V. T. Fauske, P. Burdet, P. Jokubauskas, T. Furnival, C. Francis, M. Nord, T. Ostasevicius, K. MacArthur, D. Johnstone, M. Sarahan, J. Taillon, T. Aarholt, V. Migunov, A. Eljarrat, J. Caron, T. Nemoto, T. Poon, S. Mazzucco, N. Tappy, N. Cautaerts, S. Somnath, T. Slater and M. Walls, *hyperspy/hyperspy: v2.3.0*, DOI: 10.5281/zenodo.14956374.
5. eeee, https://gitlab.au.dk/disorder/EDX-High-Entropy-Alloys).
6. A. Taylor and R. W. Floyd, *Acta Crystallogr*, 1950, **3**, 285–289.
7. S. Sasaki, K. Fujino, Tak, Eacute and Y. Uchi, *Proceedings of the Japan Academy, Series B*, 1979, **55**, 43–48.
8. K. Suzuki, T. Kaneko, H. Yoshida, H. Morita and H. Fujimori, *Journal of Alloys and Compounds*, 1995, **224**, 232–236.
9. M. A. Ahsan, O. Fernandez-Delgado, E. Deemer, H. Y. Wang, A. A. El-Gendy, M. L. Curry and J. C. Noveron, *J Mol Liq*, 2019, **290**.
10. S. Frank, M. Folkjær, M. L. N. Nielsen, M. J. Marks, H. S. Jeppesen, M. Ceccato, S. J. L. Billinge, J. Catalano and N. Lock, *J Mater Chem A*, 2024, **12**, 781–794.
11. A. Li, Y. Tong, H. H. Song and X. H. Chen, *J Phys Chem C*, 2018, **122**, 17278–17286.
12. M. Folkjær, L. F. Lundegaard, H. S. Jeppesen, M. J. Marks, M. S. Hvid, S. Frank, G. Cibin and N. Lock, *Dalton Transactions*, 2022, 10740–10750.
13. N. Prinz, S. Strubbe, M. Bauer and M. Zobel, *New J Chem*, 2023, **47**, 11623–11635.
14. Z. H. Y. Chen, Z. J. Chen, O. K. Farha and K. W. Chapman, *J Am Chem Soc*, 2021, **143**, 8976–8980.
15. C. L. Farrow, P. Juhas, J. W. Liu, D. Bryndin, E. S. Bozin, J. Bloch, T. Proffen and S. J. L. Billinge, *J Phys-Condens Mat*, 2007, **19**, 335219.
16. M. Muñoz, P. Argoul and F. Farges, *Am Mineral*, 2003, **88**, 694–700.